

Thermally Induced Vibration of a Flexible Plate with Enhanced Active Constrained Layer Damping

Yueru Guo ¹, Yongbin Guo ¹, Yongxin Zhang ¹, Liang Li ^{1,*}, Dingguo Zhang ¹, Sijia Chen ²
and Mohamed A. Eltaher ^{3,4}

¹ School of Physics, Nanjing University of Science and Technology, Nanjing 210094, China; yueruguo@njust.edu.cn (Y.G.); gyb_mechanics825@163.com (Y.G.); zhangdg419@mail.njust.edu.cn (D.Z.)

² School of Mechatronics and Energy Engineering, Ningbo Tech University, Ningbo 315100, China

³ Mechanical Engineering Department, Faculty of Engineering, King Abdulaziz University, Jeddah P.O. Box 44519, Saudi Arabia; meltaher@kau.edu.sa

⁴ Mechanical Design and Production Department, Faculty of Engineering, Zagazig University, Zagazig P.O. Box 80204, Egypt

* Correspondence: liangli@njust.edu.cn; Tel.: +86-152-5098-0315

Abstract: When spacecraft execute missions in space, their solar panels—crucial components—often need to be folded, unfolded, and adjusted at an angle. These operations can induce numerous detrimental nonlinear vibrations. This paper addresses the issues of nonlinear and thermal-coupled vibration control within the context of space-based flexible solar panel systems. Utilizing piezoelectric smart hybrid vibration control technology, this study focuses on a flexible plate augmented with an active constrained layer damping. The solar panel, under thermal field conditions, is modeled and simulated using the commercial finite element simulation software ABAQUS. The research examines variations in the modal frequencies and damping properties of the model in response to changes in the coverage location of the piezoelectric patches, their coverage rate, rotational angular velocity, and the thickness of the damping layer. Simulation results indicate that structural damping is more effective when the patches are closer to the rotation axis, the coverage area of the patches is larger, the rotational speed is lower, and the damping layer is thicker. Additionally, the effectiveness of vibration suppression is influenced by the interplay between the material shear modulus, loss factor, and specific working temperature ranges. The selection of appropriate parameters can significantly alter the system's vibrational characteristics. This work provides necessary technical references for the analysis of thermally induced vibrations in flexible solar sails under complex space conditions.

Keywords: flexible plate; EACLD; finite element simulation; vibration control; temperature field

Citation: Guo, Y.; Guo, Y.; Zhang, Y.; Li, L.; Zhang, D.; Chen, S.; Eltaher, M.A. Thermally Induced Vibration of a Flexible Plate with Enhanced Active Constrained Layer Damping. *Aerospace* **2024**, *11*, 504. <https://doi.org/10.3390/aerospace11070504>

Academic Editor: Kyungil Kong

Received: 7 May 2024

Revised: 9 June 2024

Accepted: 12 June 2024

Published: 23 June 2024



Copyright: © 2024 by the authors. Licensee MDPI, Basel, Switzerland. This article is an open access article distributed under the terms and conditions of the Creative Commons Attribution (CC BY) license (<https://creativecommons.org/licenses/by/4.0/>).

1. Introduction

In the ongoing advancement of human spaceflight technology, flexible appendages such as solar sail panels and robotic arms have been widely utilized in aerospace applications [1–5]. These flexible components exploit their foldable and deployable properties to significantly reduce the overall volume of spacecraft structures and enhance operational flexibility, thereby optimizing the launch and transportation processes of spacecraft. The application of flexible appendages also significantly enhances the adaptability and operational flexibility of spacecraft in extreme external environments. For instance, the adaptive adjustment capabilities of solar sail panels greatly improve the efficiency of solar energy utilization [6,7], while the flexibility of robotic arms supports precise spatial operations and maintenance tasks [8–11]. The deployment of these technologies enables spacecraft to perform more effective payload configuration and deployment under extreme space conditions, demonstrating the modern aerospace engineering demands for

flexibility, efficiency, and reliability, and opens new possibilities for the design and execution of future space missions, expanding new avenues for the exploration of distant celestial bodies and utilization of space resources.

Deployable solar sail panels (as shown in Figure 1), typically made from lightweight flexible materials, are connected to the central spacecraft via a hinged mechanism. When conducting space missions under extreme space conditions, this structure often exhibits significant nonlinear vibrational coupling with the spacecraft's main structure due to its low stiffness, large span, and weak damping characteristics [12–15]. Movements of the rigid main body during orbital maneuvers or attitude adjustments can induce vibrations in the flexible solar sails. These vibrations, due to the structural flexibility, nonlinear behavior at the hinge points, and the large span of the sails, display complex nonlinear characteristics. If these vibrations are not effectively controlled during precise scientific experiments or spacecraft docking tasks, they may lead to structural damage, affecting the normal functionality of the spacecraft.



Figure 1. The solar panel of a SpaceX spacecraft.

Furthermore, solar sail panels also encounter thermal coupling vibrations influenced by direct solar radiation, Earth's infrared radiation, and Earth's albedo radiation [16–19]. These thermal flows not only alter the temperature distribution of the sails but also create a temperature gradient between the sails and the spacecraft main body, thereby generating thermal stresses. These thermal stresses, coupled with structural vibrations, may trigger thermally induced vibrational coupling, further complicating the dynamic behavior of the spacecraft. For instance, thermal expansion or contraction can lead to material deformation, affecting the stiffness and natural frequencies of the structure, thereby impacting the dynamic response and stability of the entire spacecraft system.

Due to the weak damping and low modal frequency characteristics of the flexible sail structures, once these adverse vibrations occur, their attenuation is typically very slow [20–22]. This not only interferes with the satellite's spatial positioning accuracy, causing deviations in the system's rigid motion posture, but also increases the risk of structural fatigue vibrations damaging the sails, thus reducing the service life of the spacecraft's flexible appendages. In extreme cases, it could even break the support mechanisms of the sails, posing a threat to the life of extravehicular activity personnel. Consequently, the issues of dynamics and vibration control of flexible solar sails have become increasingly prominent, urgently necessitating researchers to develop more precise and efficient vibration damping methods [23,24].

Researchers have extensively studied the structural vibration control of flexible spatial components made from advanced functional materials. Common vibration-control methods include passive control, active control, and hybrid active–passive control. A technique known as Passive Constrained Layer Damping (PCLD) [25–30] involves covering the vibrating structure with ordinary constrained layers and viscoelastic material (VEM) damping layers [31,32]. This configuration suppresses vibrations by dissipating energy

through the viscoelastic material when the structure vibrates. Active Constrained Layer Damping (ACL D), a vibration control technology introduced by Baz [33–39] in the 1990s, distinguishes significantly from traditional PCLD. ACLD employs a viscoelastic material layer sandwiched between the base layer and the constrained layer, combined with active control elements (such as piezoelectric or electromagnetic actuators), to effectively suppress vibrations. This technology integrates the advantages of passive damping and active control. By applying voltage through the controller, the shear deformation angle of the viscoelastic damping layer is increased; concurrently, the piezoelectric material's inverse piezoelectric effect enhances the energy dissipation capacity of the damping layer when the structure is subjected to compression or tension. Through real-time adjustments to the structural response by the active elements, ACLD technology significantly enhances vibration reduction effects [40–43].

In the decades following the development of ACLD technology, numerous scholars have conducted in-depth research on its modeling assumptions, numerical methods, and control strategies. Kumar et al. [44] utilized Hamilton's principle and the finite element method to derive the dynamic equations for beams, proposing the addition of an isolation layer between the viscoelastic layer and the base beam to enhance the damping performance of ACLD and PCLD technologies. Liao and Wang [45–47] introduced innovative edge elements to improve the stiffness of the entire structure and further suppress vibrations—a technique known as Enhanced Active Constrained Layer Damping (EACL D). This method improves the weakening of the active control ability caused by the dissipation of the VEM layer and enhances the efficiency of the piezoelectric layer to control and constrain the structure, which has been widely applied in subsequent research. Li et al. [48] used the assumed modal method and Lagrange's equations to establish discrete rigid–flexible dynamic models for hub-beam systems equipped with EACL D in open- and closed-loop scenarios, demonstrating the effect of increased edge element stiffness on the system's natural frequency, while the addition of mass to the edge elements reduced the natural frequency. Jiang et al. [49] extended the EACL D technique to plate structures, establishing a rigid–flexible dynamic model for a rotating hub-plate system treated with EACL D, considering the coupling effects of transverse bending and in-plane stretching of the rotating EACL D plate, verifying the wide applicability of EACL D technology in different structural vibration reduction applications.

In recent years, due to the focus on thermal coupling vibration issues caused by space thermal radiation in flexible appendages, researchers have also made significant progress in the field of thermally induced vibration control. Ganesan and Pradeep [50] employed the displacement field method proposed by Khatua and Cheung, using the finite element method to analyze the natural frequencies and loss factors of sandwich beams in various temperature environments, assessing the impact of the temperature-dependent shear modulus of the core material on the buckling and vibration behavior of the beams. Javani et al. [51] explored the application of active control methods and their strategies to mitigate thermally induced vibrations in functionally graded material (FGM) circular plates under thermal shocks in different boundary conditions, influenced by thermal-induced torques, forces, and thermoelectric effects. Li et al. [52] conducted studies on thermally induced vibration suppression in rotating rigid–flexible intelligent composite beams under temperature field influence, focusing on the thermal-induced vibration suppression effects in FGM beams in longitudinal and transverse directions. Fang Yuan et al. [53] and others used EACL D treatment to study the vibration control problem under thermal load shocks in high-temperature-dependent FGM base beams, considering the temperature-dependent conditions of the viscoelastic material in the constrained layer, verifying the effectiveness of EACL D treatment in suppressing thermally induced vibrations.

This paper employs finite element simulation using ABAQUS to analyze the vibrational control of EACL D plate structures in temperature fields through varying physical parameters such as temperature, patch placement, coverage, and damping layer thickness, conducting simulation analyses to study the effects of EACL D on the vibration

suppression of flexible solar sail panels. The rest of the article is organized as follows: the description of constitutive relations for piezoelectric, viscoelastic, and active constrained layer damping are presented in Section 2. Section 3 illustrates the finite element model and its verification and the temperature dependence of the material model. The numerical results presenting the effects of the position/coverage area of piezoelectric patches, rotational angular velocity, and thickness of damping layers are discussed in Section 4. The main points and conclusions are summarized in Section 5.

2. Description of the Constitutive Relationship

2.1. Constitutive Relationship of Piezoelectric Materials

The first type of coupled equation for piezoelectric materials, with stress and electric field as variables, is represented as [54]:

$$\varepsilon_{ij} = s_{ijkl}^E \sigma_{kl} + d_{ijk} E_k \quad (1)$$

$$D_i = d_{ikl} \sigma_{kl} + \varepsilon_{ij}^{\sigma} E_j \quad (2)$$

Equation (1) indicates that the strain of piezoelectric materials is composed of two parts: one due to the stress it bears and the other is due to the electric field. The first term represents the effect of stress on strain when the electric field strength is constant, and the second term represents the effect of electric field strength on strain. Equation (2) shows that the electric displacement of piezoelectric materials is influenced by both the stress it bears and the electric field, where the first term indicates the electric displacement caused by stress and the second term represents the electric displacement caused by electric field strength when the stress is zero.

In ABAQUS, it is common to use the strain and electric field strength as independent variables, employing the second type of coupled equation for piezoelectric materials [54]:

$$\sigma_{ij} = c_{ijkl}^E \varepsilon_{kl} - e_{kij} E_k \quad (3)$$

$$D_i = e_{ikl} \varepsilon_{kl} + \lambda_{ik}^{\varepsilon} E_k \quad (4)$$

The piezoelectric material used in this paper is piezoelectric ceramic. When defining piezoelectric materials in simulation software, it is necessary to input the elastic constant matrix, the relative permittivity matrix, and the piezoelectric coefficient matrix.

$$\begin{bmatrix} \sigma_{11} \\ \sigma_{22} \\ \sigma_{33} \\ \sigma_{12} \\ \sigma_{13} \\ \sigma_{23} \end{bmatrix} = \begin{bmatrix} c_{11} & c_{12} & c_{13} & 0 & 0 & 0 \\ c_{12} & c_{11} & c_{13} & 0 & 0 & 0 \\ c_{13} & c_{13} & c_{33} & 0 & 0 & 0 \\ 0 & 0 & 0 & c_{66} & 0 & 0 \\ 0 & 0 & 0 & 0 & c_{44} & 0 \\ 0 & 0 & 0 & 0 & 0 & c_{44} \end{bmatrix} \begin{bmatrix} \varepsilon_{11} \\ \varepsilon_{22} \\ \varepsilon_{33} \\ \gamma_{12} \\ \gamma_{13} \\ \gamma_{23} \end{bmatrix} - \begin{bmatrix} 0 & 0 & e_{31} \\ 0 & 0 & e_{31} \\ 0 & 0 & e_{33} \\ 0 & 0 & 0 \\ e_{15} & 0 & 0 \\ 0 & e_{15} & 0 \end{bmatrix} \begin{bmatrix} E_1 \\ E_2 \\ E_3 \end{bmatrix} \quad (5)$$

where $c_{66} = \frac{1}{2}(c_{11} - c_{12})$.

$$\begin{bmatrix} D_1 \\ D_2 \\ D_3 \end{bmatrix} = \begin{bmatrix} 0 & 0 & 0 & 0 & e_{15} & 0 \\ 0 & 0 & 0 & 0 & 0 & e_{15} \\ e_{31} & e_{31} & e_{33} & 0 & 0 & 0 \end{bmatrix} \begin{bmatrix} \epsilon_{11} \\ \epsilon_{22} \\ \epsilon_{33} \\ \gamma_{12} \\ \gamma_{13} \\ \gamma_{23} \end{bmatrix} + \begin{bmatrix} \lambda_{11} & 0 & 0 \\ 0 & \lambda_{11} & 0 \\ 0 & 0 & \lambda_{33} \end{bmatrix} \begin{bmatrix} E_1 \\ E_2 \\ E_3 \end{bmatrix} \tag{6}$$

2.2. Constitutive Relationship of the Viscoelastic Layer

In engineering, the commonly used constitutive model to describe linear viscoelastic materials is the Prony series model. Its creep form can be expressed as [55]:

$$E(t) = E_\infty + \sum_{i=1}^n E_i e^{-t/\tau_i} \tag{7}$$

where τ_i represents the relaxation time, E_i is the corresponding relaxation modulus, and E_∞ denotes the equilibrium modulus. If using the Maxwell model to describe viscoelastic materials, its mathematical expression is [56]

$$\sigma + \frac{\eta}{E} \dot{\sigma} = \eta \dot{\epsilon} \tag{8}$$

Note that when $t = 0$, it follows that $E_0 = E_\infty + \sum E_i$, letting $m_i = E_i/E_0$, and then we have:

$$E(t) = E_0 \left(1 - \sum_{i=1}^N m_i \right) + \sum_{i=1}^N m_i E_0 e^{-t/\tau_i} \tag{9}$$

where E_∞ represents the long-term relaxation modulus; E_i is the elastic modulus of the i^{th} Maxwell model; and τ_i is the relaxation time of the i^{th} Maxwell model.

$$E = 3K(1 - 2\nu) \tag{10}$$

$$E = 2G(1 + \nu) \tag{11}$$

The shear modulus and bulk modulus can be calculated as follows:

$$G(t) = G_0 \left(1 - \sum_{i=1}^N g_i \right) + \sum_{i=1}^N g_i G_0 e^{-t/\tau_i} \tag{12}$$

$$K(t) = K_0 \left(1 - \sum_{i=1}^N k_i \right) + \sum_{i=1}^N k_i K_0 e^{-t/\tau_i} \tag{13}$$

It can be seen that, when using the Prony series model in the form of Equations (12) and (13) in ABAQUS to equivalently calculate viscoelastic materials, it is only necessary to compute G_0 (shear modulus) and K_0 (bulk modulus) from the elastic parameters E (modulus of elasticity) and ν (Poisson’s ratio) provided as input. The remaining parameters (g_i, K_i, τ_i) are the Prony series parameters that need to be input. The Prony series model of viscoelastic materials for one element has the same mathematical form as the Maxwell model.

2.3. ACLD Structure Dynamics Equation

Based on the classical modeling theory of plates, the kinetic energy expressions and potential energy expressions for the piezoelectric constrained layer, damping layer,

boundary element layer, and base layer can be derived using the energy method. The dynamic matrix can be obtained using the Lagrangian method, and the overall dynamic equation can be formed by assembly according to the finite element method as follows:

$$M\ddot{\Delta} + G\dot{\Delta} + K\Delta = Q_f \quad (14)$$

When the system moves solely under the drive of piezoelectric forces without any other external forces, the right-hand side of the above equation is zero. On this basis, the state space form can be rewritten as

$$\bar{M}\dot{z} + \bar{K}z = 0 \quad (15)$$

$$\text{where } z = \begin{bmatrix} \dot{\Delta} \\ \Delta \end{bmatrix}, \bar{M} = \begin{bmatrix} M & 0 \\ 0 & I \end{bmatrix}, \bar{K} = \begin{bmatrix} G & K \\ -I & 0 \end{bmatrix}.$$

3. Modeling and Simulation Analysis Based on ABAQUS

3.1. Model Establishment and Verification

The subject of this paper is a solar sail panel moving around a central rigid body. When modeling in finite element software, it is simplified to a thin rectangular plate model with one end fixed and the other end free. As shown in Figure 2, the model consists of a piezoelectric patch made of viscoelastic material and piezoelectric material, partially laid on the surface of a complete aluminum base plate.

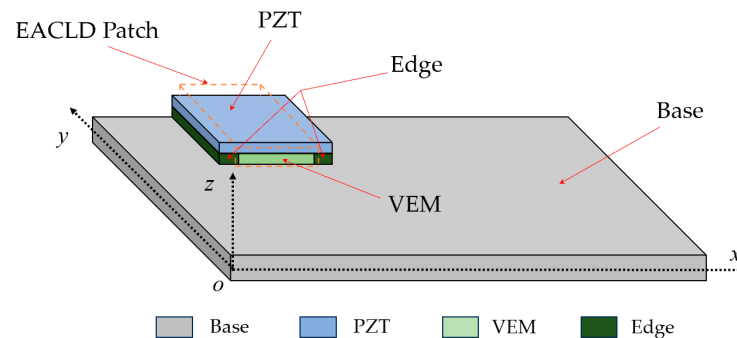


Figure 2. Schematic of the EACL D model.

To verify the accuracy of the modeling, this paper establishes the model using the same parameters as those found in the literature [57]. Additionally, it is necessary to define parameters such as the piezoelectric constants and dielectric constants of the piezoelectric material and use the Assembly module to move the components to the appropriate positions for assembly. After assembly, static analysis steps and frequency analysis steps are created in the Step module. Considering the synergistic action between components, the Tie contact type is used to bond the base layer, viscoelastic layer, and piezoelectric layer in pairs. Then, in the load application Load step, the left end of the base layer is subjected to constraints for rotation and displacement in six degrees of freedom. In the simulations conducted, the piezoelectric patches are assumed to operate under open-circuit conditions, as in the literature [57]. Finally, the established model is divided into a mesh grid. In the ACLD model, the base layer is divided into 30 columns and 10 rows on average, with a total of 300 elements. The element type is S4R, the number of nodes is 411 and the total number of variables in the model is 2466. Meanwhile, in the EACL D model, the base is divided into 16 columns and 10 rows, with a total of 160 elements. The third and sixth columns and the first to the fourth rows are edge elements; Columns 4 and 5 and 1 through 4 represent traditional ACLD elements, and the element length of the edge elements is

half that of the ACLD. The element type is S4R, the number of nodes is 231 and the total number of variables in the model is 2772. The detailed mesh is shown in Figure 3.

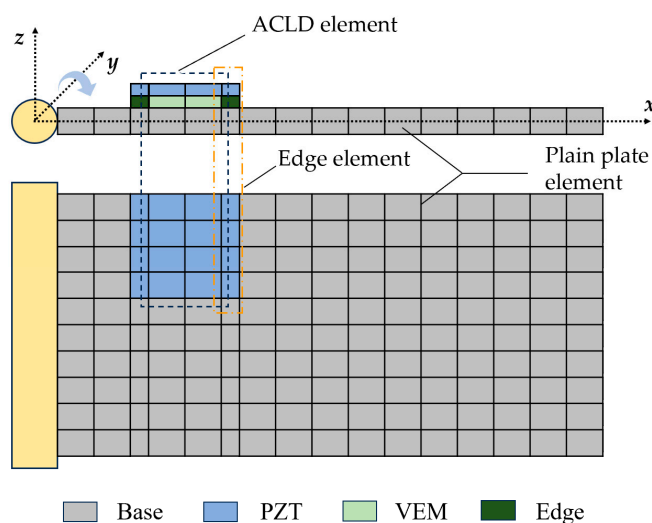


Figure 3. Detailed mesh grid of EACL model.

The first three order natural frequencies obtained from the finite element simulation software are compared with the experimental results from the literature [57]. The detailed results comparison is given in Table 1. The first and second modal shapes correspond to the first two bending modes of the model, respectively, and the third modal shape corresponds to the first torsional mode of the model. It can be seen that the natural frequencies calculated by the simulation software closely match the results obtained from the experiments in the literature, with errors all controlled within 2%, preliminarily proving the accuracy of the finite element software simulation modeling.

Table 1. Comparison of natural frequencies of the plate between experiment and simulation.

Model	Mode No.	Ref. [57]/Hz	Present/Hz	Error (%)
ACLD	1	18.00	18.31	1.70
	2	76.66	77.99	1.74
	3	106.58	108.50	1.80
EACL	1	18.37	18.35	0.11
	2	77.12	78.10	1.27
	3	107.91	109.48	1.45

3.2. Temperature Dependence of Materials

In actual engineering applications, the vibrational performance of solar sail plates is significantly influenced by different temperature fields, showing notable variations. To better observe and study the vibrational characteristics of the structure under various temperature conditions, it is necessary to describe the temperature characteristics of the different materials comprising the model separately.

It is generally considered that the parameters of the piezoelectric layer PZT material change slightly with temperature and can be neglected during modeling; the viscoelastic layer made of Dyad606, however, shows that its complex shear modulus and loss factor vary with temperature, as illustrated in Figure 4 [58]:

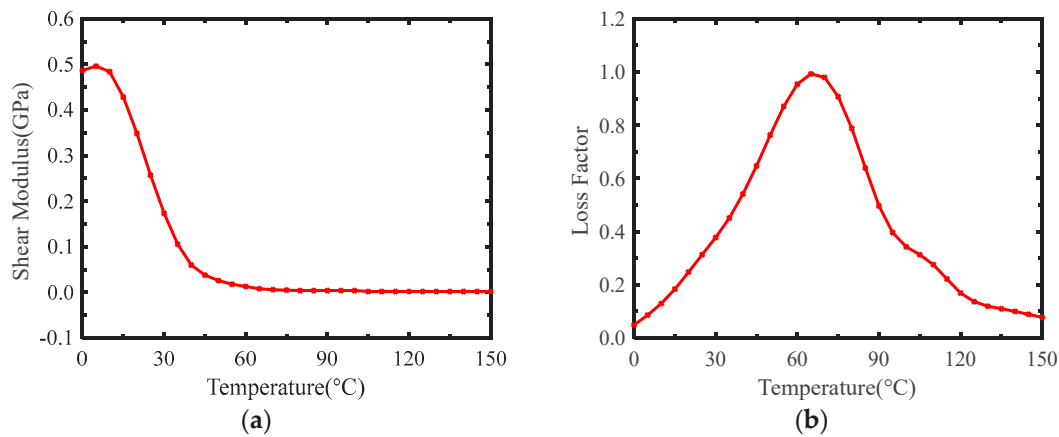


Figure 4. The variation of shear modulus and loss factor of viscoelastic layer with temperature. (a) The variation of shear modulus of Dyad606 with temperature. (b) The variation of loss factor of Dyad606 with temperature.

The base layer made of Ti-6Al-4V exhibits variations in its Young's modulus ($E_3(T)$) and thermal expansion coefficient ($k_3(T)$) with temperature. These variations are characterized using the following parametric formula:

$$P = P_0 \left(\frac{P_{-1}}{T} + 1 + P_1 T + P_2 T^2 + P_3 T^3 \right) \quad (16)$$

Here, T represents the current temperature and P denotes any variable changes in Young's modulus or thermal expansion coefficient. The constants P_{-1} , P_0 , P_1 , P_2 and P_3 are determined by fitting material property data, as listed in Table 2 for both the Young's modulus and thermal expansion coefficient [58]. In ABAQUS, these data are entered by defining the "complex modulus" of the viscoelastic material, which includes the real- and imaginary-part modulus values of the material's shear modulus and bulk modulus at different temperatures.

Table 2. Parameters of Ti-6Al-4V with temperature.

Properties	P_{-1}	P_0	P_1	P_2	P_3
E_3 / Pa	0	122.56×10^9	-4.486×10^{-4}	0	0
k_3	0	7.75788×10^{-6}	6.638×10^{-4}	-3.147×10^{-6}	0

4. Different Parameter Verification

4.1. The Influence of the Coverage Position of Piezoelectric Patches on Structural Damping Effect

In practical applications, the vibrational characteristics of structures are often affected by the coverage position of piezoelectric patches. This section discusses the impact of the coverage position of piezoelectric patches. Initially, a model of the EACL D flexible plate is established, with the temperature dependence of the materials already explained in Section 3.2. The remaining geometric parameters and material parameters are as shown in Table 3.

Table 3. Geometrical and physical parameters of a flexible plate with EACL D treatment.

Parameter	Value	Parameter	Value
L	0.3 m	ρ_1	7600 kg/m ³
L_e	0.15 m	ρ_2	1250 kg/m ³
h_1	2.54×10^{-4} m	ρ_3	4430 kg/m ³
h_2	5.08×10^{-4} m	G_2	Varies with temperature

h_3	1.89×10^{-3} m	G_{a7}	0.862
E_1	64.9 GPa	μ_1	0.33
E_2	$2(1 + \mu_2) G_2$	μ_2	0.45
E_3	Varies with temperature	μ_3	0.342
k_3	Varies with temperature	R	0 m

To better study the influence of temperature and the coverage position of piezoelectric patches on vibration characteristics under open-circuit conditions, the size of the piezoelectric patch is set to 0.06 m × 0.15 m. A dimensionless parameter l_x is introduced, representing the ratio of the distance from the left side of the patch to the pivot axis to the total length of the base layer, as shown in Figure 5. In the temperature field from 0 °C to 150 °C, with increments of 10 °C, l_x values of 0, $2/15$ and $4/15$ are considered to calculate the natural frequencies of the EACL D model as the relative position of the patch changes.

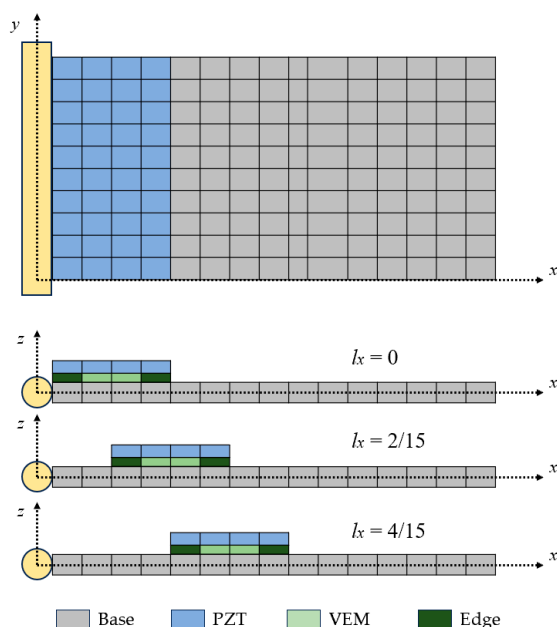


Figure 5. The variation of EACL D patch covering position.

Figures 6 and 7 show the curves of the first four natural frequencies and damping ratios as a function of temperature when l_x varies. It can be observed that, for the same coverage condition, the trend of frequency and damping ratio changes with temperature is basically the same under the same modal condition: the natural frequency decreases with the increase in temperature, while the system’s damping ratio shows a trend of first increasing and then decreasing, with an inflection point occurring in the temperature range of 60 °C to 70 °C.

For other modal conditions, at the same temperature, the structure’s natural frequency tends to decrease as the patch moves rightward. The rightward movement of the patch causes geometric changes in the structure, changing the system’s mass distribution and structural stiffness, thereby leading to changes in natural frequencies. Specifically, for the second modal condition, the natural frequencies for $l_x = 2/15$ and $l_x = 4/15$ first increase and then decrease with temperature, while for $l_x = 0$, the natural frequency unexpectedly rises. This indicates that the second modal vibration differs from other modes, being more sensitive to temperature changes and thus exhibiting different frequency variation trends.

Additionally, all three modal conditions achieve the highest natural frequency and maximum damping ratio at $l_x = 0$ (for the second modal condition, the maximum damping ratio is achieved at $l_x = 4/15$). Accordingly, we can find the best passively damped patch cover position for different modes, as shown in Table 4. Overall, the vibrational characteristics of the structure are significantly affected by changes in the position of the piezoelectric patch placement. For systems under the influence of high-frequency external excitation sources, the closer the relative position l_x is to 0, meaning the closer the left side of the piezoelectric patch is to the pivot axis, the faster the decay of the first, third, and fourth modal vibrations and the better the damping effect.

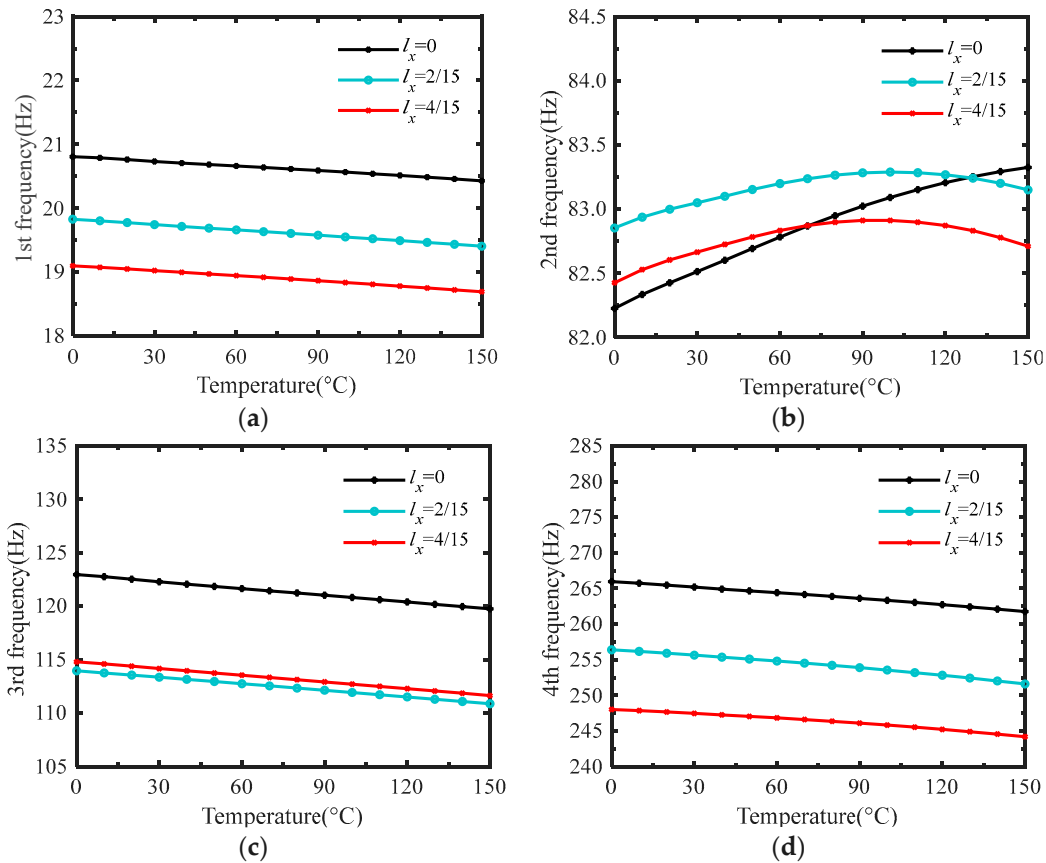
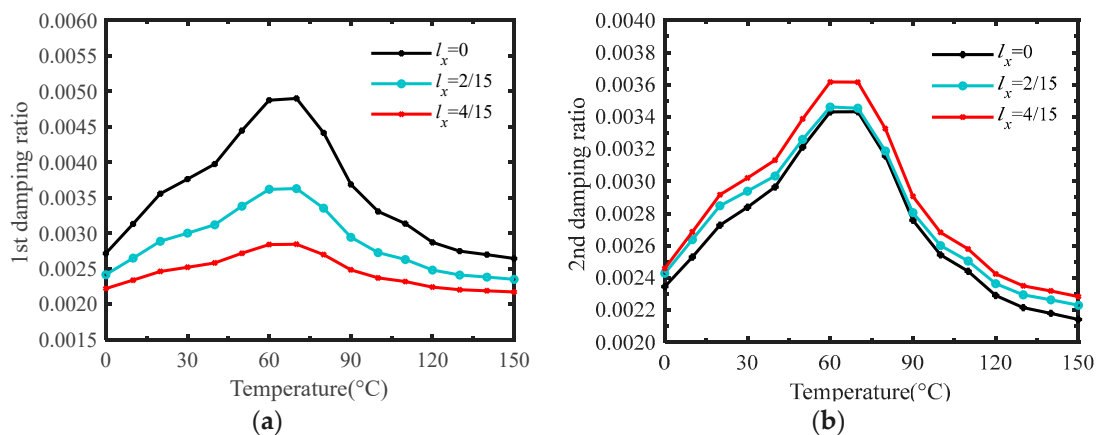


Figure 6. Variations of the first four orders of natural frequencies of the plate with different cover positions of EACL D patch with temperature. (a) First order modal frequency. (b) Second order modal frequency. (c) Third order modal frequency. (d) Fourth order modal frequency.



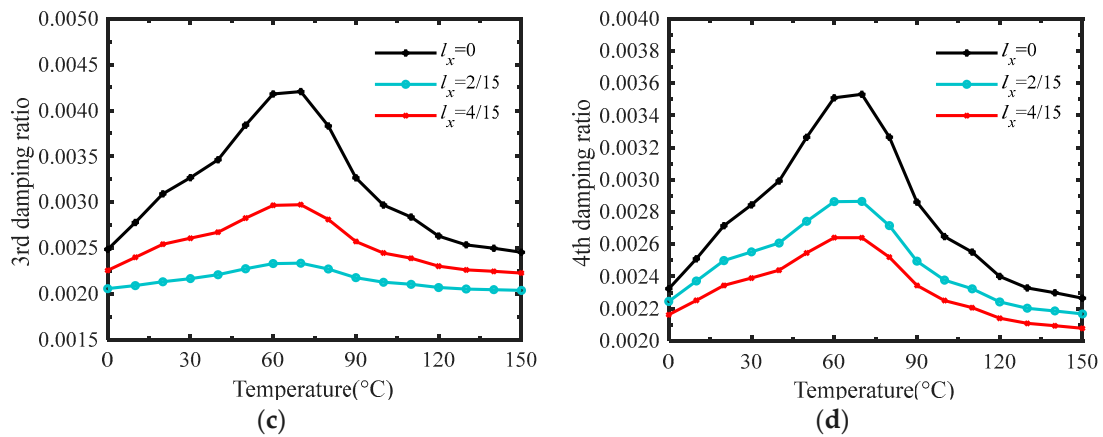


Figure 7. Variations of the first four orders of damping ratios of the plate with different cover positions of EACL D patch with temperature. (a) First order modal damping ratio. (b) Second order modal damping ratio. (c) Third order modal damping ratio. (d) Fourth order modal damping ratio.

Table 4. Patch locations for best passive damping.

Mode No.	Best Choice	Second Choice (If Available)
1	$l_x = 0$	$l_x = 2/15$
2	$l_x = 4/15$	$l_x = 2/15$
3	$l_x = 0$	$l_x = 4/15$
4	$l_x = 0$	$l_x = 2/15$

4.2. The Influence of the Coverage Ratio of Piezoelectric Patches on Structural Damping Effect

The damping characteristics of a structure are also closely related to the coverage area of the piezoelectric patches. We allowed the left end of the patch to be aligned with the pivot axis and placed on the base layer, as shown in Figure 8, varying the length of the patch along the length direction of the base layer, with all other parameters remaining consistent with Section 4.1. Simulation calculations were performed for models with coverage ratios of $4/15$, $5/15$, $6/15$ and $7/15$, respectively.

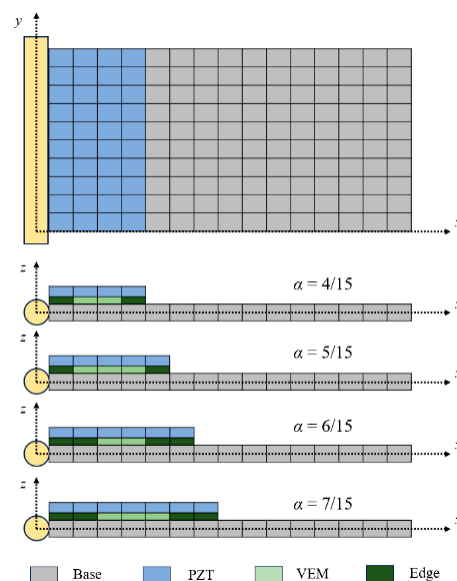


Figure 8. Schematic drawing of the coverage of EACL D patch.

Figures 9 and 10 present the curves of the first four modal natural frequencies and damping ratios as a function of temperature for models with different coverage ratios. As the temperature increases, the natural frequencies of different modalities in models of different coverage ratios generally show a decreasing trend; however, for the second mode (see Figure 9b), as the coverage ratio increases, the natural frequency of each model transitions from a singular rising trend to first rising and then falling, with the falling portion occupying an increasingly larger temperature range. This is mainly due to changes in the thermal expansion coefficient, elastic modulus, and structural damping coefficient of the viscoelastic material with increasing temperature, which reduces the stiffness of the structure and further affects the system's vibrational characteristics, leading to changes in the natural frequency. However, the second mode is less sensitive to temperature changes, resulting in the overall small changes in natural frequency and increases in certain intervals.

Furthermore, by comparing models with different coverage ratios, it can be observed that models with $4/15$ coverage ratios have similar damping ratio values and trends, as do those with $6/15$ and $7/15$, but there is a significant difference in the third mode between $6/15$ and $7/15$ coverage ratios. Figure 10 also reveals that when the temperature is below $60\text{ }^{\circ}\text{C}$, the damping ratio increases with rising temperature. However, as the temperature rises above $70\text{ }^{\circ}\text{C}$, further increases in temperature lead to a gradual decrease in the damping ratio, and the system's damping effect gradually worsens. In the temperature range of $30\text{ }^{\circ}\text{C}$ to $100\text{ }^{\circ}\text{C}$, the damping ratio is highly sensitive to temperature changes, with changes in the material's elastic modulus and internal friction effect, significantly affecting the damping effect on the vibrational system. Also, we can find the best passively damped patch coverage for the first four modes, as shown in Table 5. Therefore, in engineering design, the impact of temperature must be fully considered, and the operational temperature range of the system should be controlled reasonably to ensure the system has good vibration-control performance.

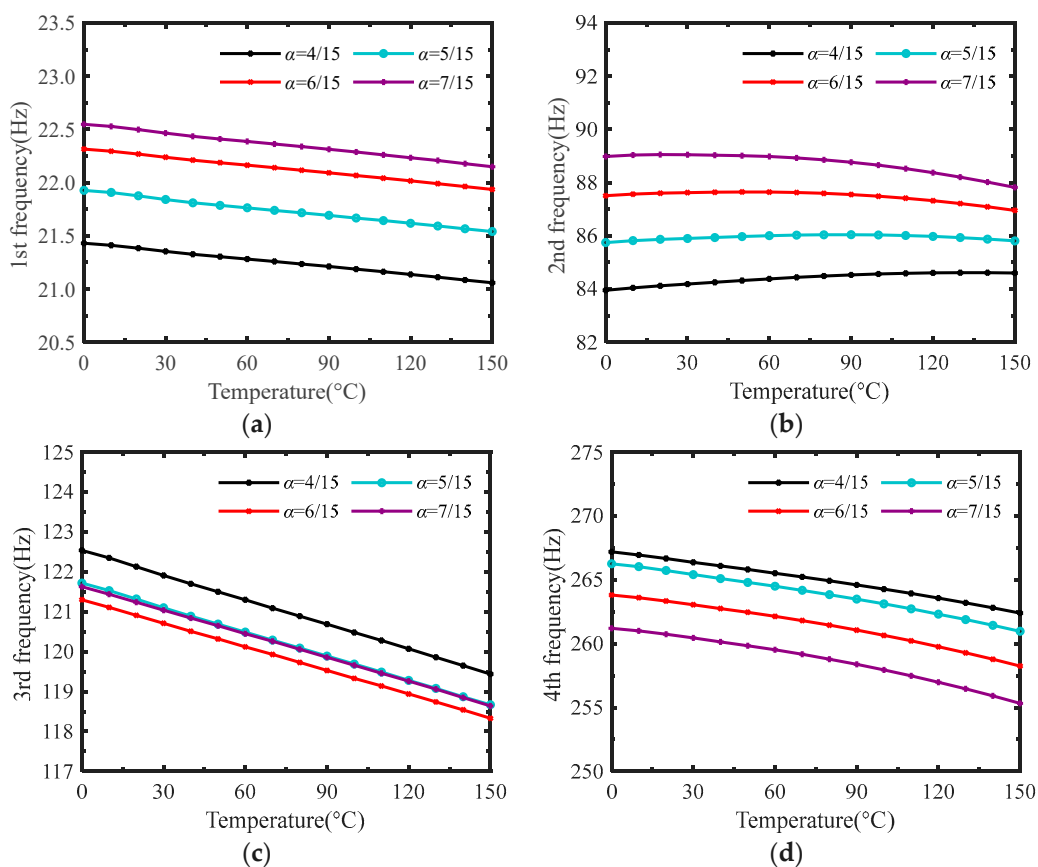


Figure 9. Variations of the first four orders of natural frequencies of the plate with different coverages of the EACLD patch treatment with temperature. (a) First order modal frequency. (b) Second order modal frequency. (c) Third order modal frequency. (d) Fourth order modal frequency.

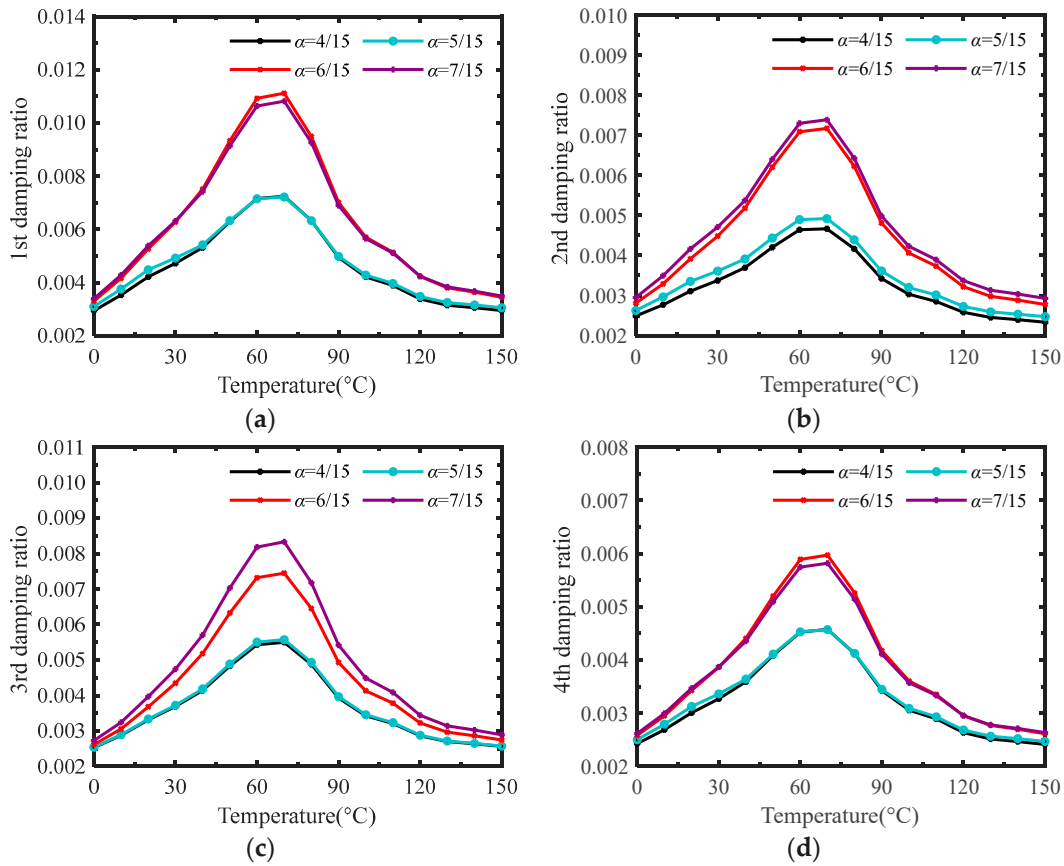


Figure 10. Variations of the first four orders of damping ratios of the plate with different coverages of the EACLD patch treatment with temperature. (a) First order modal damping ratio. (b) Second order modal damping ratio. (c) Third order modal damping ratio. (d) Fourth order modal damping ratio.

Table 5. Patch coverage for best passive damping.

Mode No.	Best Choice	Second Choice (If Available)
1	$\alpha = 6/15$	$\alpha = 7/15$
2	$\alpha = 7/15$	$\alpha = 6/15$
3	$\alpha = 7/15$	$\alpha = 6/15$
4	$\alpha = 6/15$	$\alpha = 6/15$

4.3. The Influence of Rotational Angular Velocity on Structural Damping Effect

The vibrational characteristics of structures with EACLD are also related to the structure’s rotational angular velocity. Considering a thin plate whose left end displacement and rotational angle are constrained, a 0.06 m × 0.15 m patch on it is fixed at a length of L = 0.04 m. The rotation of model around the y-axis is simulated by applying equivalent rotational body forces to the structure, with all other parameters remaining consistent with Section 4.1. Simulations are conducted in the temperature field for the structure’s modal vibrations at rotational speeds $\omega = 0$ to 6000 rpm, with intervals of 1000 rpm.

From Figure 11, it can be observed that at low rotational speeds, each modal frequency has a lower natural frequency and a higher damping ratio, indicating better damping effects at this stage. As the rotational speed increases, the natural frequencies gradually rise, and the damping ratios gradually decrease, weakening the system’s damping

effect. This is because low rotational speeds entail smaller dynamic loads, with the stiffness of the structure dominating at this stage, leading to relatively strong internal friction and energy dissipation. As the rotational speed increases, greater inertial forces act on each mass element, increasing the system's equivalent stiffness. At the same time, the material and structure's non-linear properties become more pronounced, leading to increased natural frequencies and reduced damping effects.

Figure 11b shows that the second modal frequencies of models at different rotational speeds exhibit a similar trend: with increasing temperature, the natural frequency first increases slowly to a certain temperature point and then decreases, with this temperature threshold interval being approximately between 100 and 120 °C, indicating significant material temperature dependence within this range. Observing Figure 12b, it can also be found that the second modal damping ratios at different rotational speeds have almost identical values and trends, showing that the system's dynamic response and excitation exhibit linear characteristics. This means that the damping characteristics of the second mode are mainly influenced by the system's inherent properties and structural qualities, rather than by the rotational speed, leading to relative stability in the damping ratio across the studied range of rotational speeds.

Especially from Figure 11, it can be noted that at lower rotational speeds (1000 rpm), the pattern of changes in the natural frequencies of the structure's modalities is essentially consistent with that of the model without applied rotational speed (0 rpm). This implies that for this system, adopting lower rotational speeds is an effective method for reducing the natural frequencies of the structure. Additionally, we can find the suitable rotational speeds for different modes of vibration control, as shown in Table 6. In conclusion, to control the vibrational state of specific modes of rotating flexible plates, it is necessary to select appropriate rotational angular velocities and specific operational temperature ranges.

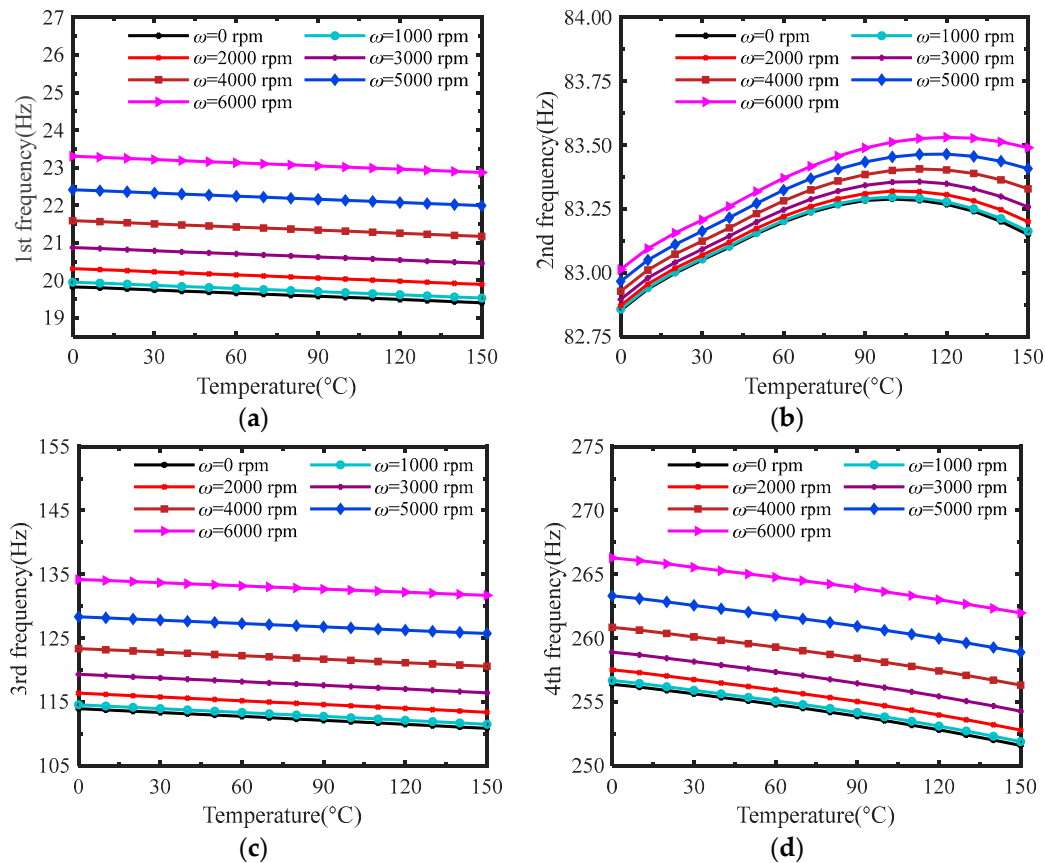


Figure 11. Variations of the first four orders of natural frequencies of the plate with EACL D treatment with temperature at different rotational speeds. (a) First order modal frequency. (b) Second order modal frequency. (c) Third order modal frequency. (d) Fourth order modal frequency.

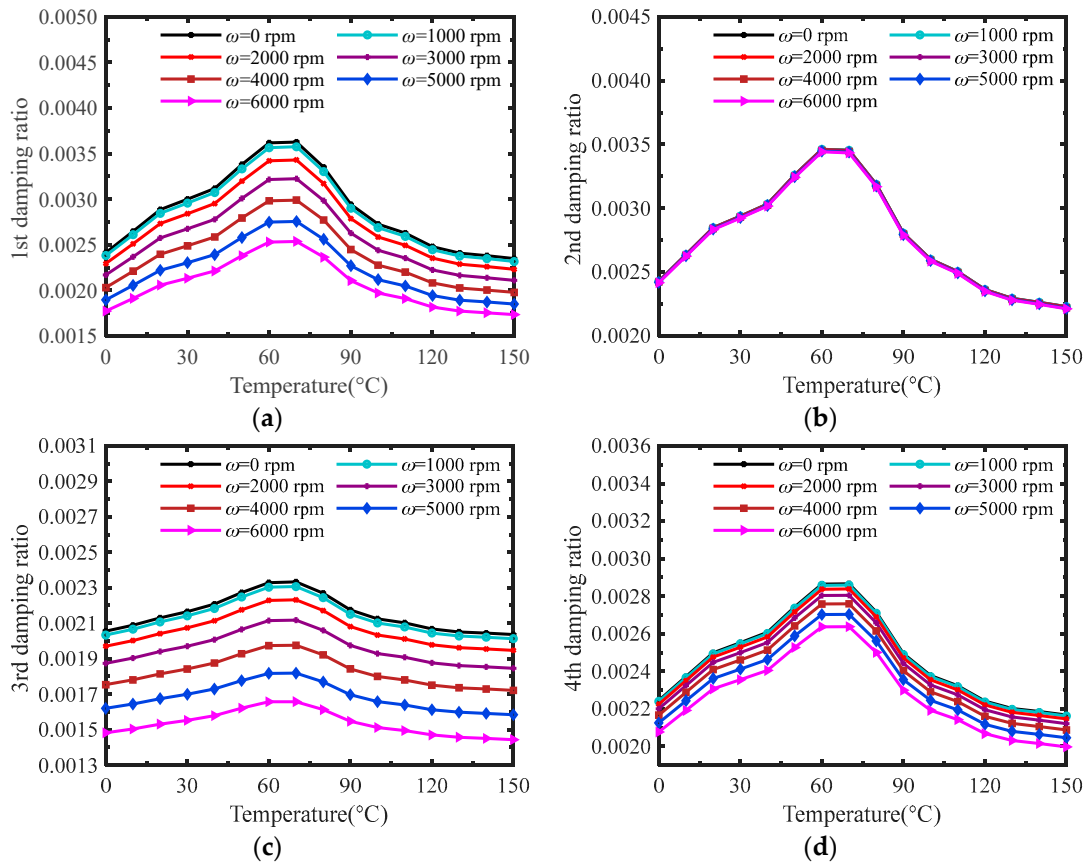


Figure 12. Variations of the first four orders of damping ratios of the plate with EACL treatment with temperature at different rotational speeds. (a) First order modal damping ratio. (b) Second order modal damping ratio. (c) Third order modal damping ratio. (d) Fourth order modal damping ratio.

Table 6. Rotational speeds for best passive damping.

Mode No.	Best Choice	Second Choice (If Available)
1	$\omega = 0$ rpm	$\omega = 1000$ rpm
2	ω From 0 to 6000 rpm	ω From 0 to 6000 rpm
3	$\omega = 0$ rpm	$\omega = 1000$ rpm
4	$\omega = 0$ rpm	$\omega = 1000$ rpm

4.4. The Influence of Damping Layer Thickness on Structural Damping Effect

The thickness of the damping layer also significantly impacts the structure’s damping effect. To make the simulation results more universally applicable, a dimensionless parameter $h_v = h_2/h_3$ representing the ratio of the viscoelastic layer’s thickness to the base layer’s thickness is defined, where h_2 is the viscoelastic layer thickness and h_3 is the base layer thickness. Five different cases are considered ($h_v = 0.4, 0.8, 1.2, 1.6$ and 2.0) for simulation calculations and analysis of the EACL rotating flexible plate model.

From Figure 13, it can be observed that under any value of h_v , the natural frequency of the same mode generally shows a decreasing trend as the temperature increases. At the same temperature, as the viscoelastic layer becomes thicker, the system’s first, second, and fourth modal natural frequencies gradually increase, with the damping ratio showing a similar trend; for the third mode, the natural frequency tends to decrease with the increasing thickness of the viscoelastic layer at the same temperature. This is because the modal frequencies of the system are influenced by the structure’s elasticity and mass distribution.

As the viscoelastic layer becomes thicker, it increases the system's total mass and the energy dissipation caused by internal friction, thus affecting the system's modal frequency response and damping effect. From Figure 14, it is evident that regardless of temperature changes, for the second and fourth modal vibrations, the damping ratio always increases with the thickening of the viscoelastic layer. For the first and third modal vibrations, the damping ratios in the cases of $h_v = 1.2, 1.6$ and $h_v = 2.0$ are very close, and $h_v = 1.6$ has a larger damping ratio peak, indicating that at this time, the thickness of the viscoelastic layer has a smaller impact on damping performance, and the damping ratio is not sensitive to changes in the thickness. This implies that in engineering applications, if the aim is to suppress vibrations of different modal orders, the choice of damping layer thickness should be made flexibly according to the actual situation (see Table 7), as blindly increasing the thickness of the damping layer is not always the optimal solution.

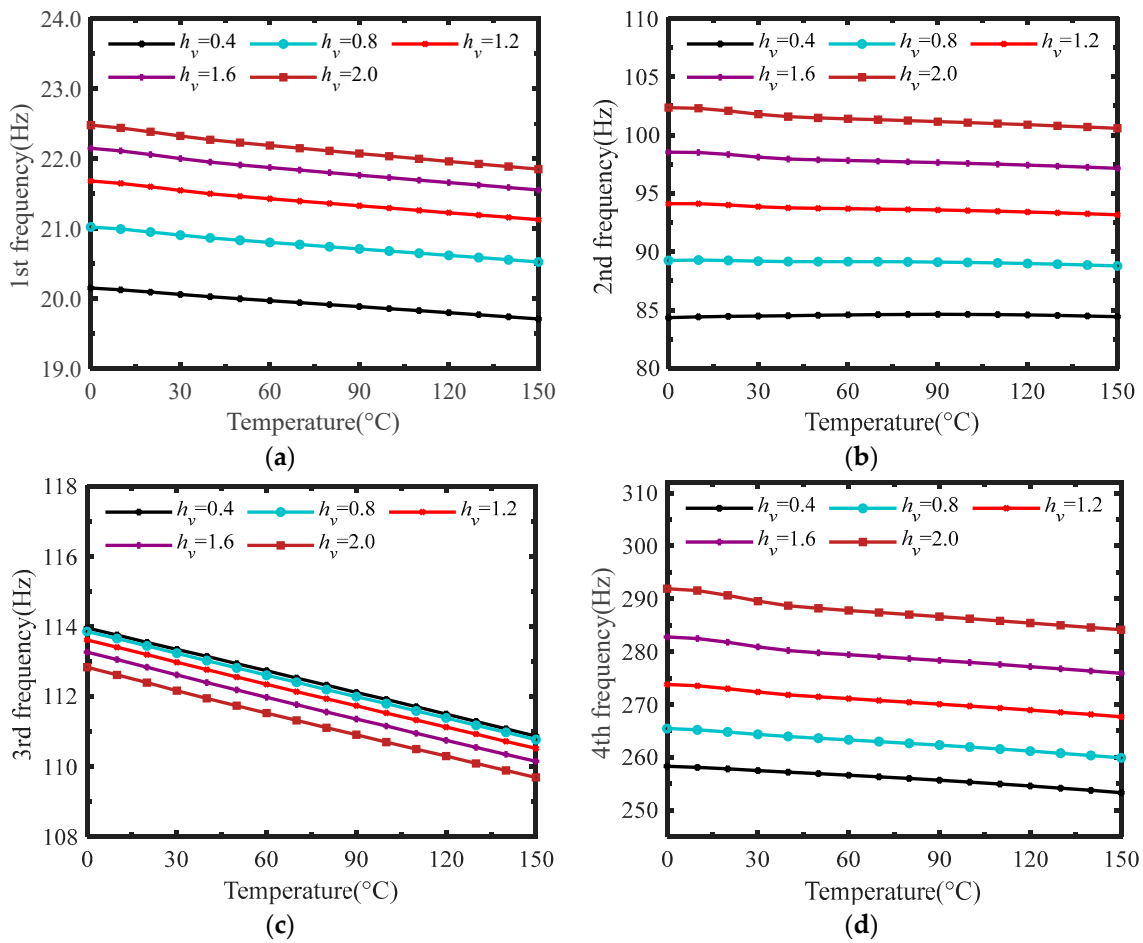


Figure 13. Variations of the first four orders of natural frequencies of the plate with EACL D treatment with temperature under different thicknesses of damping layer. (a) First order modal frequency. (b) Second order modal frequency. (c) Third order modal frequency. (d) Fourth order modal frequency.

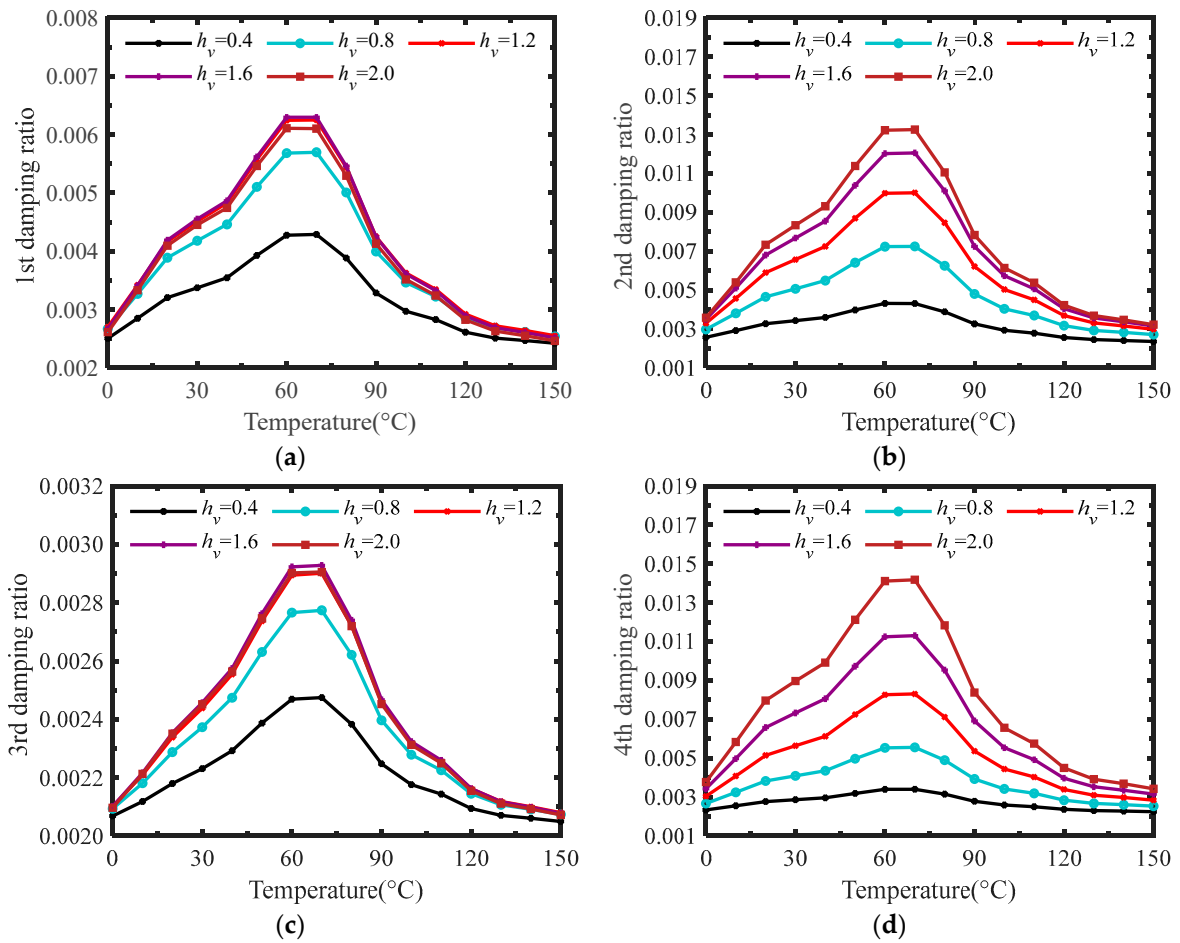


Figure 14. Variations of the first four orders of damping ratios of the plate with EACL D treatment with temperature under different thicknesses of damping layer. (a) First order modal damping ratio. (b) Second order modal damping ratio. (c) Third order modal damping ratio. (d) Fourth order modal damping ratio.

Table 7. Thickness of damping layer for best passive damping.

Mode No.	Best Choice	Second Choice (If Available)
1	$h_v = 1.2$ OR $h_v = 1.6$	$h_v = 2.0$
2	$h_v = 2.0$	$h_v = 1.6$
3	$h_v = 1.6$	$h_v = 1.2$ OR $h_v = 2.0$
4	$h_v = 2.0$	$h_v = 1.6$

5. Conclusions

This paper conducted a vibration analysis of EACL D plate structures considering the temperature field using ABAQUS. By simulating the model through variations in physical parameters such as temperature, patch position, coverage ratio, and damping layer thickness, the study investigated the vibration-damping effect of EACL D on flexible solar sail panels, leading to the following conclusions:

1. Position and Coverage Area of Piezoelectric Patches: The research indicates that increasing the coverage area of piezoelectric patches near the rotation axis by 20% can enhance the damping efficiency by up to 15%.
2. Temperature Effects: The results demonstrate that as the ambient temperature increases from 20 °C to 100 °C, the system’s natural frequency may decrease by 5% to 10%, while the damping ratio significantly increases in certain modes, particularly peaking between 60 °C and 70 °C.

3. Effects of Rotational Speed: With an increase in rotational speed from 1000 rpm to 5000 rpm, the modal frequency rises approximately 3% to 7%, whereas the corresponding damping ratio decreases by 5% to 10%.
4. By increasing the thickness of the damping layer from 0.76 mm to 2.27 mm, the structure exhibits improved damping performance in the temperature range of 40 °C to 100 °C, with nearly a 20% increase in the damping ratio.

Author Contributions: Conceptualization, L.L. and Y.G. (Yueru Guo); methodology, Y.G. (Yueru Guo) and Y.G. (Yongbin Guo); resources, Y.G. (Yongbin Guo) and M.A.E.; software, visualization and writing—original draft preparation, Y.G. (Yueru Guo); supervision, D.Z. and S.C.; funding acquisition, D.Z. and L.L., writing—review and editing, Y.G. (Yueru Guo) and Y.Z. All authors have read and agreed to the published version of the manuscript.

Funding: This research was funded by the National Undergraduate Training program for Innovation and Entrepreneurship, grant number 202210288103, the National Natural Science Foundation of China, grant numbers 12072159 and 12232012 and the Fundamental Research Funds for the Central Universities, grant number 30922010314.

Data Availability Statement: The data that support the findings of this study are available from the corresponding author upon reasonable request. The data are not publicly available due to restrictions.

Acknowledgments: We would like to thank the faculty of Physics in the Nanjing University of Science and Technology for their generous help with this simulation.

Conflicts of Interest: The authors declare no conflicts of interest.

References

1. Ellery, A. An Engineering Approach to the Dynamic Control of Space Robotic On-Orbit Servicers. *Proc. Inst. Mech. Eng. Part G J. Aerosp. Eng.* **2004**, *218*, 79–98. <https://doi.org/10.1243/0954410041321998>.
2. Gasbarri, P.; Monti, R.; Campolo, G.; Toglia, C. Control-Oriented Modelization of a Satellite with Large Flexible Appendages and Use of Worst-Case Analysis to Verify Robustness to Model Uncertainties of Attitude Control. *Acta Astronaut.* **2012**, *81*, 214–226. <https://doi.org/10.1016/j.actaastro.2012.07.016>.
3. Sabatini, M.; Monti, R.; Gasbarri, P.; Palmerini, G. Deployable Space Manipulator Commanded by Means of Visual-Based Guidance and Navigation. *Acta Astronaut.* **2013**, *83*, 27–43. <https://doi.org/10.1016/j.actaastro.2012.10.015>.
4. Gasbarri, P.; Pisculli, A. Dynamic/Control Interactions between Flexible Orbiting Space-Robot during Grasping, Docking and Post-Docking Manoeuvres. *Acta Astronaut.* **2015**, *110*, 225–238. <https://doi.org/10.1016/j.actaastro.2015.01.024>.
5. van Woerkom, P.T.L.M.; Misra, A.K. Robotic Manipulators in Space: A Dynamics and Control Perspective. *Acta Astronaut.* **1996**, *38*, 411–421. <https://doi.org/10.1016/0094-576500018-5>.
6. Cassenti, B.N.; Matloff, G.L.; Strobl, J. The Structural Response and Stability of Interstellar Solar Sails. *J. Br. Interplanet. Soc.* **1996**, *49*, 345–350.
7. Wright, J.L. *Space Sailing*; Taylor & Francis: Abingdon, UK, 1992; ISBN 2-88124-842-X.
8. Yan, X.; Shan, M.; Shi, L. Adaptive and Intelligent Control of a Dual-Arm Space Robot for Target Manipulation during the Post-Capture Phase. *Aerosp. Sci. Technol.* **2023**, *142*, 108688. <https://doi.org/10.1016/j.ast.2023.108688>.
9. Yokokohji, Y.; Toyoshima, T.; Yoshikawa, T. Efficient Computational Algorithms for Trajectory Control of Free-Flying Space Robots with Multiple Arms. *IEEE Trans. Robot. Autom.* **1993**, *9*, 571–580.
10. Rutkovskii, V.Y.; Sukhanov, V.M.; Glumov, V.M. Motion Equations and Control of the Free-Flying Space Manipulator in the Reconfiguration Mode. *Autom. Remote Control* **2010**, *71*, 70–86.
11. Ishijima, Y.; Tzeranis, D.; Dubowsky, S. The On-Orbit Maneuvering of Large Space Flexible Structures by Free-Flying Robots. In Proceedings of the 8th International Symposium on Artificial Intelligence, Robotics and Automation in Space, Munich, Germany, 5–8 Septmeber 2005; pp. 1–6.
12. Asadi, D.; Farsadi, T. Active Flutter Control of Thin Walled Wing-Engine System Using Piezoelectric Actuators. *Aerosp. Sci. Technol.* **2020**, *102*, 105853. <https://doi.org/10.1016/j.ast.2020.105853>.
13. Xu, C.; Zhou, H.; Mao, Y. Analysis of Vibration and Noise Induced by Unsteady Flow inside a Centrifugal Compressor. *Aerosp. Sci. Technol.* **2020**, *107*, 106286. <https://doi.org/10.1016/j.ast.2020.106286>.
14. Jafari-Talookolaei, R.-A.; Abedi, M.; Attar, M. In-Plane and out-of-Plane Vibration Modes of Laminated Composite Beams with Arbitrary Lay-Ups. *Aerosp. Sci. Technol.* **2017**, *66*, 366–379. <https://doi.org/10.1016/j.ast.2017.02.027>.
15. Zhang, L.; Ding, S.-J.; Xie, Y.; Xu, Y.M.; Yuan, Q.L.; Ji, S.-M. Study of Active Vibration Control for Fiber Smart Beam. *Procedia Eng.* **2011**, *15*, 897–902. <https://doi.org/10.1016/j.proeng.2011.08.166>.
16. Chai, Y.-Y.; Song, Z.-G.; Li, F.-M. Active Aerothermoelastic Flutter Suppression of Composite Laminated Panels with Time-Dependent Boundaries. *Compos. Struct.* **2017**, *179*, 61–76.

17. Lin, B.C.; Xie, T.F.; Xu, M.; Li, Y.H.; Yang, J. Natural Frequencies and Dynamic Responses of Rotating Composite Non-Uniform Beams with an Elastically Root in Hygrothermal Environment. *Compos. Struct.* **2019**, *209*, 968–980.
18. Wang, Z.-X.; Shen, H.-S. Nonlinear Vibration of Sandwich Plates with FG-GRC Face Sheets in Thermal Environments. *Compos. Struct.* **2018**, *192*, 642–653.
19. Khosravi, S.; Arvin, H.; Kiani, Y. Vibration Analysis of Rotating Composite Beams Reinforced with Carbon Nanotubes in Thermal Environment. *Int. J. Mech. Sci.* **2019**, *164*, 105187.
20. Fu, B.; Sperber, E.; Eke, F. Solar Sail Technology—A State of the Art Review. *Prog. Aerosp. Sci.* **2016**, *86*, 1–62. <https://doi.org/10.1016/j.paerosci.2016.07.001>.
21. Gong, H.; Gong, S.; Liu, D. Attitude Dynamics and Control of Solar Sail with Multibody Structure. *Adv. Space Res.* **2022**, *69*, 609–619. <https://doi.org/10.1016/j.asr.2021.10.012>.
22. Scholz, C.; Romagnoli, D.; Dachwald, B.; Theil, S. Performance Analysis of an Attitude Control System for Solar Sails Using Sliding Masses. *Adv. Space Res.* **2011**, *48*, 1822–1835. <https://doi.org/10.1016/j.asr.2011.05.032>.
23. Chen, T.-Z.; Liu, X.; Cai, G.-P.; You, C.-L. Attitude and Vibration Control of a Solar Sail. *Adv. Space Res.* **2023**, *71*, 4557–4567. <https://doi.org/10.1016/j.asr.2023.01.039>.
24. Johnson, L.; Young, R.; Montgomery, E.; Alhorn, D. Status of Solar Sail Technology within NASA. *Adv. Space Res.* **2011**, *48*, 1687–1694. <https://doi.org/10.1016/j.asr.2010.12.011>.
25. Swallow, W. An Improved Method of Damping Panel Vibrations. *Br. Pat. Specif.* **1939**, *513*, 171.
26. Nokes, D.S.; Nelson, F.C. Constrained Layer Damping with Partial Coverage. *Shock Vib. Bull.* **1968**, *38*, 5–12.
27. Kerwin, E.M., Jr. Damping of Flexural Waves by a Constrained Viscoelastic Layer. *J. Acoust. Soc. Am.* **1959**, *31*, 952–962.
28. Mead, D.J.; Markus, S. The Forced Vibration of a Three-Layer, Damped Sandwich Beam with Arbitrary Boundary Conditions. *J. Sound Vib.* **1969**, *10*, 163–175.
29. Cai, C.; Zheng, H.; Liu, G.R. Vibration Analysis of a Beam with PCLD Patch. *Appl. Acoust.* **2004**, *65*, 1057–1076. <https://doi.org/10.1016/j.apacoust.2004.05.004>.
30. Lall, A.K.; Asnani, N.T.; Nakra, B.C. Vibration and Damping Analysis of Rectangular Plate with Partially Covered Constrained Viscoelastic Layer. *J. Vib. Acoust.* **1987**, *109*, 241–247.
31. Wang, T.; Xu, C.; Guo, N.; Hamdaoui, M.; Daya, E.M. Uncertainty propagation of frequency response of viscoelastic damping structures using a modified high-dimensional adaptive sparse grid collocation method. *Mech. Adv. Mater. Struct.* **2022**, *29*, 506–524.
32. Kpeky, F.; Abed-Meraim, F.; Daya, E.M.; Samah, O.D. Modeling of hybrid vibration control for multilayer structures using solid-shell finite elements. *Mech. Adv. Mater. Struct.* **2018**, *25*, 1033–1046.
33. Ray, M.C.; Oh, J.; Baz, A. Active Constrained Layer Damping of Thin Cylindrical Shells. *J. Sound Vib.* **2001**, *240*, 921–935. <https://doi.org/10.1006/jsvi.2000.3287>.
34. Baz, A.; Tempia, A. Active Piezoelectric Damping Composites. *Sens. Actuators A Phys.* **2004**, *112*, 340–350. <https://doi.org/10.1016/j.sna.2004.01.021>.
35. Arafa, M.; Baz, A. Energy-Dissipation Characteristics of Active Piezoelectric Damping Composites. *Compos. Sci. Technol.* **2000**, *60*, 2759–2768. <https://doi.org/10.1016/S0266-353800090-7>.
36. Ray, M.C.; Baz, A. Optimization of Energy Dissipation of Active Constrained Layer Damping Treatments of Plates. *J. Sound Vib.* **1997**, *208*, 391–406. <https://doi.org/10.1006/jsvi.1997.1171>.
37. Baz, A.; Ro, J. Optimum Design and Control of Active Constrained Layer Damping. *ASME J. Mech. Des.* **1995**, *117*, 135–144. <https://doi.org/10.1115/1.2836447>.
38. Baz, A. Robust Control of Active Constrained Layer Damping. *J. Sound Vib.* **1998**, *211*, 467–480. <https://doi.org/10.1006/jsvi.1997.1315>.
39. Park, C.H.; Baz, A. Vibration Control of Bending Modes of Plates Using Active Constrained Layer Damping. *J. Sound Vib.* **1999**, *227*, 711–734. <https://doi.org/10.1006/jsvi.1999.2391>.
40. Hau, L.C.; Fung, E.H.K. Effect of ACLD Treatment Configuration on Damping Performance of a Flexible Beam. *J. Sound Vib.* **2004**, *269*, 549–567. [https://doi.org/10.1016/S0022-460X\(03\)00041-5](https://doi.org/10.1016/S0022-460X(03)00041-5).
41. Li, L.; Zhang, D.; Guo, Y. Dynamic Modeling and Analysis of a Rotating Flexible Beam with Smart ACLD Treatment. *Compos. Part B Eng.* **2017**, *131*, 221–236. <https://doi.org/10.1016/j.compositesb.2017.07.050>.
42. Vasques, C.M.A.; Dias Rodrigues, J. Active Vibration Control of Smart Piezoelectric Beams: Comparison of Classical and Optimal Feedback Control Strategies. *Comput. Struct.* **2006**, *84*, 1402–1414. <https://doi.org/10.1016/j.compstruc.2006.01.026>.
43. Vasques, C.M.A.; Dias Rodrigues, J. Combined Feedback/Feedforward Active Control of Vibration of Beams with ACLD Treatments: Numerical Simulation. *Comput. Struct.* **2008**, *86*, 292–306. <https://doi.org/10.1016/j.compstruc.2007.01.027>.
44. Kumar, S.; Kumar, R.; Sehgal, R. Enhanced ACLD Treatment Using Stand-off-Layer: FEM Based Design and Experimental Vibration Analysis. *Appl. Acoust.* **2011**, *72*, 856–872. <https://doi.org/10.1016/j.apacoust.2011.05.010>.
45. Liao, W.H.; Wang, K.W. Characteristics of Enhanced Active Constrained Layer Damping Treatments with Edge Elements, Part 1: Finite Element Model Development and Validation. *J. Vib. Acoust.* **1998**, *120*, 886–893. <https://doi.org/10.1115/1.2893916>.
46. Liao, W.H.; Wang, K.W. Characteristics of Enhanced Active Constrained Layer Damping Treatments with Edge Elements: Part II—System Analysis. In Proceedings of the International Design Engineering Technical Conferences and Computers and Information in Engineering Conference, Sacramento, CA, USA, 14–17 September 1997; American Society of Mechanical Engineers: New York, NY, USA, 1997; Volume 80401, p. V01AT02A005.

47. Liao, W.H.; Wang, K.W. A New Active Constrained Layer Configuration with Enhanced Boundary Actions. *Smart Mater. Struct.* **1996**, *5*, 638.
48. Li, L.; Liao, W.-H.; Zhang, D.; Guo, Y. Dynamic Modeling and Analysis of Rotating Beams with Partially Covered Enhanced Active Constrained Layer Damping Treatment. *J. Sound Vib.* **2019**, *455*, 46–68. <https://doi.org/10.1016/j.jsv.2019.04.026>.
49. Jiang, F.; Li, L.; Liao, W.-H.; Zhang, D. Vibration Control of a Rotating Hub-Plate with Enhanced Active Constrained Layer Damping Treatment. *Aerosp. Sci. Technol.* **2021**, *118*, 107081. <https://doi.org/10.1016/j.ast.2021.107081>.
50. Ganesan, N.; Pradeep, V. Buckling and Vibration of Sandwich Beams with Viscoelastic Core under Thermal Environments. *J. Sound Vib.* **2005**, *286*, 1067–1074. <https://doi.org/10.1016/j.jsv.2005.01.043>.
51. Javani, M.; Eslami, M.R.; Kiani, Y. Active Control of Thermally Induced Vibrations of Temperature-Dependent FGM Circular Plate with Piezoelectric Sensor/Actuator Layers. *Aerosp. Sci. Technol.* **2024**, *146*, 108997. <https://doi.org/10.1016/j.ast.2024.108997>.
52. Li, L.; Liao, W.-H.; Zhang, D.; Guo, Y. Vibration Analysis of a Free Moving Thin Plate with Fully Covered Active Constrained Layer Damping Treatment. *Compos. Struct.* **2020**, *235*, 111742. <https://doi.org/10.1016/j.compstruct.2019.111742>.
53. Fang, Y.; Li, L.; Zhang, D.; Chen, S.; Liao, W.-H. Vibration Suppression of a Rotating Functionally Graded Beam with Enhanced Active Constrained Layer Damping Treatment in Temperature Field. *Thin-Walled Struct.* **2021**, *161*, 107522. <https://doi.org/10.1016/j.tws.2021.107522>.
54. Wang, J.; Su, W.; Wang, C.; Gai, Z. *Piezoelectric Vibration Theory and Applications*; Science Press: Beijing, China, 2011; pp. 15–17.
55. Barbero, E.J.; Barbero, E.J. *Finite Element Analysis of Composite Materials Using Abaqus®*, 2nd ed.; CRC Press: Boca Raton, FL, USA, 2023; ISBN 978-1-00-310815-3.
56. Pettermann, H.E.; Cheyrou, C.; DeSimone, A. Modeling and Simulation of Anisotropic Linear Viscoelasticity. *Mech. Time-Depend. Mater.* **2021**, *25*, 679–689. <https://doi.org/10.1007/s11043-020-09468-8>.
57. Dai, R. Modeling and Implementation of Plates with Enhanced Active Constrained Layer Damping. Master's Thesis, The Chinese University of Hong Kong, Hong Kong, China, 2004.
58. Guo, Y.; Li, L.; Zhang, D. Dynamic Modeling and Vibration Analysis of Rotating Beams with Active Constrained Layer Damping Treatment in Temperature Field. *Compos. Struct.* **2019**, *226*, 111217. <https://doi.org/10.1016/j.compstruct.2019.111217>.

Disclaimer/Publisher's Note: The statements, opinions and data contained in all publications are solely those of the individual author(s) and contributor(s) and not of MDPI and/or the editor(s). MDPI and/or the editor(s) disclaim responsibility for any injury to people or property resulting from any ideas, methods, instructions or products referred to in the content.